ELSEVIER

Journal of Computational and Applied Mathematics 132 (2001) 191–210

JOURNAL OF COMPUTATIONAL AND APPLIED MATHEMATICS

www.elsevier.nl/locate/cam

A numerical study of mixed parabolic–gradient systems

J.G. Verwer *, B.P. Sommeijer

Centre for Mathematics and Computer Science (CWI), P.O. Box 94079, 1090 GB Amsterdam, The Netherlands

Received 5 January 2000; received in revised form 22 May 2000

Abstract

This paper is concerned with the numerical solution of parabolic equations coupled with gradient equations. The gradient equations are ordinary differential equations whose solutions define positions of particles in the spatial domain of the parabolic equations. The vector field of the gradient equations is determined by gradients of solutions to the parabolic equations. Such mixed parabolic–gradient systems are for example, used in neurobiological studies of the formation of axonal connections in the nervous system. We discuss a numerical approach for solving parabolic–gradient systems on a grid. The basic ingredients are the fourth-order spatial finite differencing for the parabolic equations, piecewise cubic Hermite interpolation for approximating the gradient equations, and explicit time-stepping by means of a Runge–Kutta–Chebyshev method.

Keywords: Parabolic equations; Gradient equations; Computational neuroscience

1. Introduction

The mathematical model motivating our work emanates from a neurobiological study in Hentschel and Van Ooyen [7] on the development of neuronal connections in the nervous system, in particular, outgrowth of axons from neurons in a developmental phase. Growth of axons to their targets is partly guided by concentration gradients of biochemical molecules in the extracellular space. These gradients arise from diffusion and chemical interactions and vary in space and time. The diffusion processes, the chemical interactions and the positions of the growth cones of axons, are modelled by systems of parabolic equations with source terms coupled with gradient equations. The gradient equations are ordinary differential equations and define positions of the axonal growth cones.

This paper deals with numerical methods. We discuss a general approach for solving parabolic–gradient systems on a grid. For spatial discretization we use the fourth-order finite differencing for the parabolic equations and piecewise cubic Hermite interpolation for approximating the gradient

* Corresponding author.

E-mail addresses: jan.verwer@cwi.nl (J.G. Verwer), b.p.sommeijer@cwi.nl (B.P. Sommeijer).

0377-0427/01/$ - see front matter
PII: S0377-0427(00)00605-1

equations. This spatial discretization leaves us with a semi-discrete system whose time integration is the main subject of our study. Because the semi-discrete gradient equations are nonstiff, and locally defined and nonlinear, explicit integration is attractive. On the other hand, the semi-discrete parabolic problems are stiff and therefore cannot be efficiently solved with a standard explicit method.

For time integration, we examine the explicit Runge–Kutta–Chebyshev (RKC) method. This method originates from [8] and has been designed for the time integration of systems of ordinary differential equations which have a 'close-to-normal' Jacobian matrix with eigenvalues located in a long, narrow band along the negative axis in the complex plane (see also [11,14]). Many semi-discrete parabolic partial differential equations fulfil this property. RKC is based on a family of second-order consistent RKC formulas with a real stability boundary approximately equal to $0.65s^2$, where $s \geqslant 2$ denotes the number of stages. Hence, the real stability boundary is quadratic in s. Noteworthy is that s can vary and can be made arbitrarily large to fulfil the stability requirement for a chosen step size. This makes it possible for RKC to select at each step the most efficient step size (maximal) defined by local error control [11], as well as the most efficient stable formula (minimal s). This also makes it possible to use RKC for a march to steady state, provided s can be kept within reasonable bounds for efficiency. Moreover, RKC evaluates the explicit formulas in just a few vectors of storage. These characteristics of the method make it especially attractive for parabolic problems in several spatial variables. Because we wish to integrate the gradient equations explicitly, it is interesting to examine RKC for mixed parabolic–gradient systems.

The contents is as follows. In Section 2, we outline the mixed parabolic–gradient system taking the system from [7] as an example. Section 3 is devoted to the Hermite interpolation procedure. Since in this paper we restrict ourselves to numerical illustrations in two spatial dimensions, we only discuss the 2D interpolant adopting the style in [12]. Spatial discretization aspects are dealt with in Section 4. In Section 5, we derive a simple model for linear time-stepping stability for which we examine power boundedness for Runge–Kutta methods. Section 6 is devoted to the RKC method. We examine its stability, briefly discuss its convergence for the approximate gradient equations, and illustrate its performance as a variable stepsize solver using the code from [11]. In Section 7, we mention possibilities for future research on parabolic–gradient systems.

2. A mixed parabolic–gradient system

The model from [7] has been designed to admit an analytical–numerical treatment. It should be considered as a first prototype for more realistic models which undoubtedly will require a full numerical approach. In this section, we will briefly outline the model from [7], in particular, some properties of the gradient equation. The numerical methods discussed in later sections are applicable to this special model and easily allow generalizations on the model side.

The model contains parabolic equations of the type

$$\frac{\partial \rho_l}{\partial t} = d_l \Delta \rho_l - \delta_l \rho_l + S_l, \quad t > 0, \quad \boldsymbol{x} \in \Omega \subset \mathbb{R}^m, \tag{1}$$

where $\rho_l(\boldsymbol{x},t)$ represents the concentration of a chemical l at the spatial point $\boldsymbol{x}$ and time t. The chemical l is either a chemoattractant or a chemorepellant. For further use, we introduce the notations $\rho_{l,\mathrm{a}}$ and $\rho_{l,\mathrm{r}}$ for attractants and repellants, respectively. Boundary conditions play no special role so that we may assume that we have a pure initial value problem or periodic boundary conditions. For

numerical convenience we impose periodicity and put $\Omega = [0,1]^m$. The coefficients d_l and δ_l are positive constants and S_l is a source flux. The source flux may depend on other chemicals, released at the so-called fixed-target points $\in \Omega$ or at moving points $\boldsymbol{r}_n(t) \in \Omega$ representing the position of the growth cone of axon n at time t. Source terms are typically strongly localized or even delta-like. Omitting the index n for convenience of notation, $\boldsymbol{r}(t)$ is a solution of the gradient equation

$$\frac{\mathrm{d}\boldsymbol{r}}{\mathrm{d}t} = \sum_l \lambda_{l,\mathrm{a}} \nabla \rho_{l,\mathrm{a}}(\boldsymbol{r}(t),t) - \sum_l \lambda_{l,\mathrm{r}} \nabla \rho_{l,r}(\boldsymbol{r}(t),t), \quad t > 0, \tag{2}$$

where $\boldsymbol{r}(0) = \boldsymbol{r}_0$ and $\lambda_{l,\mathrm{a}}$ and $\lambda_{l,\mathrm{r}}$ are positive constants. For given concentration gradients, (2) is a standard initial value problem for an autonomous system of ordinary differential equations $\dot{\boldsymbol{r}} = \boldsymbol{f}(\boldsymbol{r})$. The parabolic equations (1) and the gradient equations (2) are coupled through the sources S_l. More general parabolic or gradient equations leading to stronger coupling are conceivable. For example, the coefficients $\lambda_{l,\mathrm{a}}$ and $\lambda_{l,\mathrm{r}}$ could be made dependent on concentrations and positions.

Let us recall some properties of gradient equations. Consider, for simplicity, the equation

$$\frac{\mathrm{d}\boldsymbol{r}}{\mathrm{d}t} = \lambda \nabla \rho(\boldsymbol{r}(t),t), \quad t > 0, \quad \boldsymbol{r}(0) = \boldsymbol{r}_0, \tag{3}$$

based on a single concentration ρ and a constant λ being either positive or negative. The Jacobian matrix is the symmetric $m \times m$ matrix composed of the second-order spatial derivatives of ρ. Hence, if ρ is at least twice continuously differentiable, we have Lipschitz continuity guaranteeing existence and uniqueness of solutions. From (3) we deduce

$$\begin{aligned}\frac{\mathrm{d}}{\mathrm{d}t}\rho(\boldsymbol{r}(t),t) &= \lambda \nabla \rho(\boldsymbol{r}(t),t) \cdot \nabla \rho(\boldsymbol{r}(t),t) + \frac{\partial}{\partial t}\rho(\boldsymbol{r}(t),t) \\ &= \lambda ||\nabla \rho(\boldsymbol{r}(t),t)||^2 + \frac{\partial}{\partial t}\rho(\boldsymbol{r}(t),t).\end{aligned} \tag{4}$$

Consequently, for negative (positive) λ the concentration will eventually decrease (increase) along a solution of the gradient equation in the approach to a stationary concentration field. Hence, for a stationary concentration field, extremal points (zero gradient vector) are limit points. Maxima are stable if $\lambda > 0$ and unstable if $\lambda < 0$. At minima, the situation is reversed, stability if $\lambda < 0$ and instability if $\lambda > 0$. Saddle points are always unstable. In the application, one assumes that solutions ρ of the parabolic equations converge to a stationary solution so that the above observations apply.

The gradient equation (2) describes the combined effect of a growth cone growing up gradients of attractants and growing down gradients of repellants. Associate to (2) the auxiliary concentration

$$\Phi = \sum_l \lambda_{l,\mathrm{a}} \rho_{l,\mathrm{a}} - \sum_l \lambda_{l,\mathrm{r}} \rho_{l,\mathrm{r}}. \tag{5}$$

Then (2) is rewritten as

$$\frac{\mathrm{d}\boldsymbol{r}}{\mathrm{d}t} = \nabla \Phi(\boldsymbol{r}(t),t), \quad t > 0, \quad \boldsymbol{r}(0) = \boldsymbol{r}_0. \tag{6}$$

Hence, in the approach to steady state, maxima of Φ are stable limit points of (6) and minima are always unstable. For an extensive discussion on gradient equation properties, see [13].

2.1. Example

The model in [7] is based on three species, a target-derived attractant ρ_1, an axon-derived attractant ρ_2 and an axon-derived repellant ρ_3. The target-derived attractant is released at N_t fixed target points $\boldsymbol{x}_n$. The two axon-derived species are released at N_a moving positions $\boldsymbol{r}_n(t)$. Typically, in simulations N_a and N_t range from about 10 to 50. Hence, we have three coupled parabolic equations

$$\frac{\partial \rho_1}{\partial t} = d_1 \Delta \rho_1 - \delta_1 \rho_1 + S_1(\boldsymbol{x}, \{\boldsymbol{x}_n\}, \rho_1, \rho_2, \rho_3), \tag{7}$$

$$\frac{\partial \rho_2}{\partial t} = d_2 \Delta \rho_2 - \delta_2 \rho_2 + S_2(\boldsymbol{x}, \{\boldsymbol{r}_n\}, \rho_1, \rho_2, \rho_3), \tag{8}$$

$$\frac{\partial \rho_3}{\partial t} = d_3 \Delta \rho_3 - \delta_3 \rho_3 + S_3(\boldsymbol{x}, \{\boldsymbol{r}_n\}, \rho_1, \rho_2, \rho_3), \tag{9}$$

subjected to given initial functions at $t = 0$ and coupled to the N_a initial value problems

$$\frac{\mathrm{d}\boldsymbol{r}_n}{\mathrm{d}t} = \lambda_1 \nabla \rho_1(\boldsymbol{r}_n(t), t) + \lambda_2 \nabla \rho_2(\boldsymbol{r}_n(t), t) - \lambda_3 \nabla \rho_3(\boldsymbol{r}_n(t), t), \tag{10}$$

where $\boldsymbol{r}_n(0) = \boldsymbol{r}_{n,0}$ and $n = 1, \ldots, N_a$. For the sake of generality, we here let the S_k depend on all three concentrations. The target-derived attractants serve to control guidance of axons to the target points. The axon-derived attractants and repellants serve to control axon bundling and debundling, respectively. In a simulation, one should start from given initial concentration fields and given initial positions $\boldsymbol{r}_n(0)$ appropriately chosen in Ω, one for each axon. The simulation is then to be continued up to a time at which all growth cones have reached a target point $\boldsymbol{x}_n$ (for innervation) and the attractant and repellant fields have become stationary. Van Ooyen [9] estimates the maximal distance between start positions and targets in axonal growth during development to be about 1.0 mm. At greater distances, the growth cones cannot sense gradients of target derived chemoattractants. Hence, 1.0 mm is a reasonable unit as length scale for the spatial domain Ω. The various diffusion constants approximately vary between 10^{-5} and $10^{-3}\,\mathrm{mm^2\,s^{-1}}$. The growth rates for the axons approximately lie between 10^{-6} and $10^{-4}\,\mathrm{mm\,s^{-1}}$, yielding maximal periods of 10^4–10^6 s to travel a distance of 1 mm. Hence, axonal growth simulation may involve very long-time intervals.

We should remark that axonal growth simulation models are still in an early state of development. Biologically, the process of target-derived attraction is now fairly well established. The working of axon derived attractions and repellants seems plausible, but there is less direct evidence. Hentschel and Van Ooyen [7] give a nice example of a successful simulation of axon development in the presence of all three diffusible fields (see [7, Fig. 1]). This simulation is based on a quasi-steady-state approximation for the parabolic equations and on an analytical solution of the resulting elliptic equations. The quasi-steady-state approximation makes sense if the axonal growth is much slower than the speed at which the concentration gradients are set up. This often seems to be true. The use of analytical solutions is of course a genuine restriction. As it is, the model seems rather sensitive for simulating bundling and debundling. The various coefficients and source terms must be chosen with real care to obtain, subsequently, bundling, debundling, target point attraction and finally complete steady state. Imposing the quasi-steady-state approximation of course simplifies matters.

3. Hermite interpolation

Let Ω_h denote a uniform space grid on Ω with grid size h and knots (x_i, y_j) (assuming two space dimensions). We wish to interpolate $\rho(\boldsymbol{x},t)$, $\boldsymbol{x}=(x,y)$, in grid cells

$$\Omega_{ij}=\{(x,y)|\, x_{i-1}\leqslant x\leqslant x_i,\, y_{j-1}\leqslant y\leqslant y_j\} \tag{11}$$

by means of two-dimensional Hermite interpolation. The Hermite interpolant on Ω_{ij} is the unique bicubic polynomial [4,12]

$$P_{\rho,ij}(\boldsymbol{x},t)=\sum_{m,n=0}^{3}\gamma_{mn}(t)(x-x_{i-1})^m(y-y_{j-1})^n, \tag{12}$$

which at the four corner points fits the values of

$$\rho,\quad \frac{\partial\rho}{\partial x},\quad \frac{\partial\rho}{\partial y},\quad \frac{\partial^2\rho}{\partial x\,\partial y}. \tag{13}$$

This means the matrix $\Gamma=(\gamma_{mn})$ is given by $\Gamma=HKH^{\mathrm{T}}$, where [12, p. 31]

$$K=\begin{pmatrix} B_{i-1,j-1} & B_{i-1,j}\\ B_{i,j-1} & B_{i,j}\end{pmatrix},\quad B_{l,k}=\begin{pmatrix} \rho(\boldsymbol{x}_{lk},t) & \rho_y(\boldsymbol{x}_{lk},t)\\ \rho_x(\boldsymbol{x}_{lk},t) & \rho_{xy}(\boldsymbol{x}_{lk},t)\end{pmatrix},$$

$\boldsymbol{x}_{lk}=(x_l,y_k)$ and

$$H=\begin{pmatrix} 1 & 0 & 0 & 0\\ 0 & 1 & 0 & 0\\ -3h^{-2} & -2h^{-1} & 3h^{-2} & -h^{-1}\\ 2h^{-3} & h^{-2} & -2h^{-3} & h^{-2}\end{pmatrix}.$$

Let $\theta=(x-x_{i-1})/h$ and $\eta=(y-y_{j-1})/h$. Taylor expansion at (x_{i-1},y_{j-1}) gives

$$\rho(\boldsymbol{x},t)-P_{\rho,ij}(\boldsymbol{x},t)=\tfrac{1}{24}\left(\theta^2(\theta-1)^2\rho_{xxxx}+\eta^2(\eta-1)^2\rho_{yyyy}\right)h^4+\mathrm{O}(h^5),$$

revealing order 4 if ρ is sufficiently differentiable. The leading error constant is rather small, being bounded by the cell center maximum $\frac{1}{384}(|\rho_{xxxx}|+|\rho_{yyyy}|)$. The error depends on the location in the grid cell, implying that upon grid refinement the order behaviour will be somewhat erratic when examining a fixed location. The Taylor expansion reveals that in the remainder term only derivatives of order 5 and higher are present. It also reveals that in the leading error term the derivatives ρ_{xyyy}, ρ_{xxxy} and ρ_{xxyy} are eliminated. A fourth-order error bound valid for nonuniform Cartesian grids can be found in [12]. In this bound, the derivatives ρ_{xxxx}, ρ_{yyyy} and ρ_{xxyy} are present.

Let $P_\rho(\boldsymbol{x},t)$ denote the piecewice bicubic polynomial on Ω obtained by connecting all cell polynomials $P_{\rho,ij}(\boldsymbol{x},t)$. The functions

$$P_\rho,\quad \frac{\partial P_\rho}{\partial x},\quad \frac{\partial P_\rho}{\partial y},\quad \frac{\partial^2 P_\rho}{\partial x\,\partial y}$$

are continuous across grid cells, so that P_ρ is C^1 on Ω. When ρ is four times continuously differentiable in space, the interpolant P_ρ is fourth-order accurate and $\partial P_\rho/\partial x$ and $\partial P_\rho/\partial y$ provide third-order approximations. In 3D, the same procedure can be applied using a 3D, Hermite interpolant. In exactly the same manner Hermite interpolation can be used on nonuniform Cartesian grids

(see [12]). Hence, a uniform grid Ω is not necessary allowing the possibility of locally refined Cartesian grids.

Next consider, for simplicity, again the gradient equation (3) and write

$$\begin{aligned}\frac{\mathrm{d}\boldsymbol{r}}{\mathrm{d}t} &= \lambda\nabla P_\rho(\boldsymbol{r}(t),t) + (\lambda\nabla\rho(\boldsymbol{r}(t),t) - \lambda\nabla P_\rho(\boldsymbol{r}(t),t))\\ &= \lambda\nabla P_\rho(\boldsymbol{r}(t),t) + \mathrm{O}(h^3).\end{aligned} \tag{14}$$

Omitting the $\mathrm{O}(h^3)$-term yields the approximate gradient equation

$$\frac{\mathrm{d}\boldsymbol{r}}{\mathrm{d}t} = \lambda\nabla P_\rho(\boldsymbol{r}(t),t), \tag{15}$$

using the same notation for solution $\boldsymbol{r}$ for convenience. This approximate gradient equation approximates its original counterpart (3) with third-order spatial accuracy. It is obvious that the more general gradient equation (2) can be approximated in the same way and that the gradient equation property (4) carries over to P_ρ. The approximate solution $\boldsymbol{r}$ and its first derivative are continuous in the whole of Ω yielding a smooth trajectory at the passing of grid cell boundaries. We note that global interpolation, e.g., cubic splines, would yield an even smoother trajectory. However, global interpolation is more expensive, and redundant, since we only need to approximate the gradient equation at a few single cells Ω_{ij}.

4. Spatial discretization

Before choosing a spatial discretization, we first make the following observation. The Hermite interpolant P_ρ discussed in the preceding section, uses finite-difference approximations of the involved derivatives, which in turn are based on semi-discrete concentration values. When inspecting the interpolant one can see that its fourth-order is maintained when applied to a semi-discrete concentration field which is at least fourth-order accurate.

Now, consider the parabolic problem (1) (for convenience of notation we here omit the index l). On Ω_h the Laplacian is approximated using the fourth-order difference stencil

$$[-1 \quad 16 \quad -30 \quad 16 \quad -1]/(12h^2). \tag{16}$$

This stencil can also be used near the boundaries due to the periodic boundary conditions. By spatial discretization we thus approximate (1) on Ω_h by the ordinary differential equation

$$\frac{\mathrm{d}\rho_h}{\mathrm{d}t} = d\Delta_h\rho_h - \delta\rho_h + S_h, \tag{17}$$

where ρ_h is the approximation to ρ on Ω_h and S_h represents the source term S on the grid. In the Hermite interpolated gradient equation (15), we have to replace, at the corner points of grid cells, the true values (13) by approximate values defined from the grid function ρ_h. This incurs a second approximation error for the gradient equation. We use the fourth-order difference stencil

$$[1 \quad -8 \quad 0 \quad 8 \quad -1]/(12h), \tag{18}$$

and denote the resulting, spatially discrete, gradient equation by

$$\frac{\mathrm{d}\boldsymbol{r}_h}{\mathrm{d}t} = \lambda\nabla P_{\rho_h}(\boldsymbol{r}_h(t),t). \tag{19}$$

The third-order accuracy is maintained because we use fourth-order difference stencils. Also the gradient equation property carries over. Because of the cross derivative, 36 grid points are involved (in 2D) in computing P_{ρ_h} for a grid cell. Convenient is that the periodic boundary conditions allow the use of stencil (18) also at cells near boundaries.

To sum up, the use of the cubic Hermite interpolation procedure and the fourth-order difference stencils (16) and (18) provides us with third-order spatial accuracy for the mixed, semi-discrete system (17), (19), i.e.,

$$\rho_h(\boldsymbol{x},t) - \rho(\boldsymbol{x},t) = \mathrm{O}(h^3), \quad \boldsymbol{r}_h(t) - \boldsymbol{r}(t) = \mathrm{O}(h^3).$$

In the gradient equation, we lose one order because we differentiate the interpolant. In the parabolic equation, we lose one order through the $\boldsymbol{r}$-dependence of the source term. This order result extends to more general mixed parabolic–gradient systems. When assessing spatial accuracy, one should keep in mind that due to the interpolation the spatial-order behaviour will normally be somewhat erratic upon grid refinement. For time integration, it is important to note that only the solution $\boldsymbol{r}_h$ and its first derivative are continuous across grid cells. We shall pay attention to this point in Section 6.4.1.

4.1. Numerical illustration

We will illustrate the spatial accuracy behaviour for the single-species system

$$\frac{\partial \rho}{\partial t} = 2\,10^{-4}\,\Delta\rho - 10^{-4}\rho + 0.2\mathrm{e}^{-200(x-0.5)^2-200(y-0.5)^2}, \quad t > 0, \tag{20}$$

$$\frac{\mathrm{d}\boldsymbol{r}_n}{\mathrm{d}t} = 10^{-2}\,\nabla\rho(\boldsymbol{r}_n(t),t), \quad t > 0, \ n = 1,\ldots,10, \tag{21}$$

with $0 \leqslant x,\ y \leqslant 1$, the zero initial function for ρ, and the initial solutions for $\boldsymbol{r}_n$ positioned on a circle with center point $(\frac{1}{2},\frac{1}{2})$ and radius 0.34,

$$\boldsymbol{r}_n(0) = \left(\tfrac{1}{2} + 0.34\cos(\tfrac{1}{5}n\pi), \tfrac{1}{2} + 0.34\sin(\tfrac{1}{5}n\pi)\right), \quad n = 1,\ldots,10.$$

The solution $\rho(\boldsymbol{x},t)$ is circle symmetric. The constant source creates a bell-shaped profile with a maximum at $(\frac{1}{2},\frac{1}{2})$. We consider the solution on the time interval $[0,100]$ during which ρ remains practically zero on the boundary. The maximum at $(\frac{1}{2},\frac{1}{2})$ acts as target point for all $\boldsymbol{r}_n(t)$. Due to the circle symmetry, all solutions $\boldsymbol{r}_n(t)$ travel along straight lines from their initial circle position to their joint target point and hence frequently cross cell boundaries with a slope. Due to the bell-shaped profile, initially they move very slowly. At time $t = 100$, the target point has been reached. Observe that the $\boldsymbol{r}_n$ are not present in the source term. For the current illustration, this means no restriction. Fig. 1 shows all 10 positions at times $t = 40, 45, 100$ and the corresponding trajectories.

We have solved system (20)–(21) in high temporal accuracy for grid sizes $h = \frac{1}{20}, \frac{1}{40}, \frac{1}{80}$ and $\frac{1}{320}$. The resulting ρ_h-fields and $r_{n,h}(t)$-values for the coarse grids were then compared with their counterparts for the fine grid, considering these as reference solutions. Table 1 lists maximum norm spatial errors at times $t = 40$ and 45. The errors for ρ_h reveal the common fourth-order convergence (the source term does not depend on the solutions of the gradient equations). Noteworthy, is that the gradient equations are solved in high accuracy, in spite of the somewhat erratic convergence behaviour upon grid refinement. As mentioned in Section 3, this behaviour is inherent to interpolation. Note that at $t = 40$ the errors in the gradient equation solutions are much smaller than at $t = 45$.

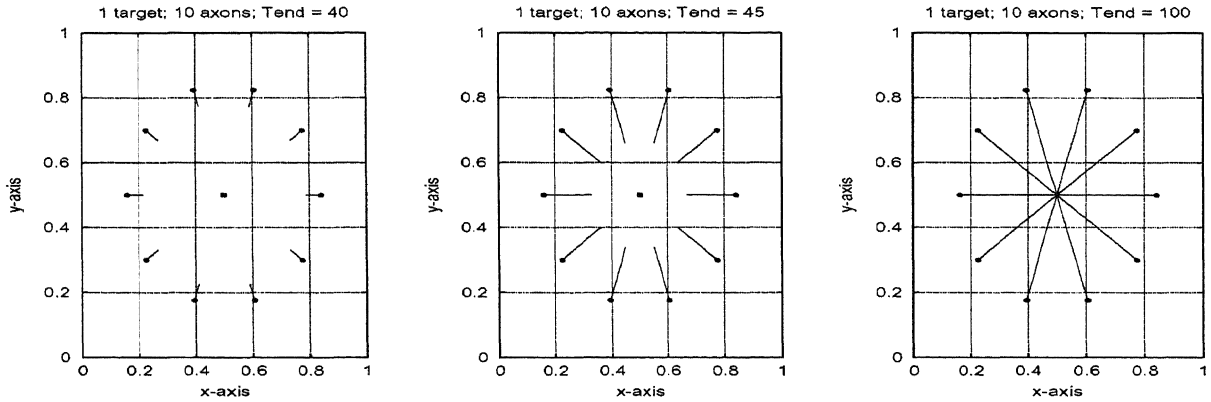

Fig. 1. Gradient equation solutions for the test problem of Section 4.1.

Table 1
Maximum norm spatial errors at $t = 40, 45$ for the test problem of Section 4.1

h	$\|(\rho - \rho_h)(40)\|$	$\|(r_n - r_{n,h})(40)\|$	$\|(\rho - \rho_h)(45)\|$	$\|(r_n - r_{n,h})(45)\|$
1/20	$0.274 \cdot 10^{-1}$	$0.254 \cdot 10^{-2}$	$0.277 \cdot 10^{-1}$	$0.234 \cdot 10^{-1}$
1/40	$0.192 \cdot 10^{-2}$	$0.137 \cdot 10^{-3}$	$0.194 \cdot 10^{-2}$	$0.116 \cdot 10^{-2}$
1/80	$0.126 \cdot 10^{-3}$	$0.778 \cdot 10^{-6}$	$0.127 \cdot 10^{-3}$	$0.970 \cdot 10^{-5}$

This is due to the fact that at $t = 40$ the positions are still close to the boundary, where $\nabla\rho$ is much smaller than at $t = 45$.

5. Stability analysis

We are now ready to discuss the time integration and begin with some stability considerations. For that purpose, we use the coupled system (7)–(10) with a few simplifying assumptions. To begin with, we suppose zero decay terms, equal diffusion coefficients and consider one gradient equation. These restrictions are nonessential for what follows. Denote $\vec{\rho} = (\rho_1, \rho_2, \rho_3)^T$ and $\vec{S} = (S_1, S_2, S_3)^T$ and rewrite system (7)–(10) as

$$\frac{\partial \vec{\rho}}{\partial t} = d\,\Delta\vec{\rho} + \vec{S}(\boldsymbol{r}, \vec{\rho}), \tag{22}$$

$$\frac{\mathrm{d}\boldsymbol{r}}{\mathrm{d}t} = \lambda_1 \nabla\rho_1(\boldsymbol{r}(t), t) + \lambda_2 \nabla\rho_2(\boldsymbol{r}(t), t) - \lambda_3 \nabla\rho_3(\boldsymbol{r}(t), t), \tag{23}$$

where we have suppressed the dependence of $\vec{S}$ on the independent variables t and $\boldsymbol{x}$. We rely on standard linear stability arguments, hence linearize along a given solution, freeze coefficients and drop constant terms. An elementary calculation yields the following constant coefficient model

system for linear stability:

$$\frac{\partial \vec{\rho}}{\partial t} = d\Delta\vec{\rho} + \boldsymbol{G}\cdot\boldsymbol{r} + \boldsymbol{S}'\vec{\rho}, \tag{24}$$

$$\frac{\mathrm{d}\boldsymbol{r}}{\mathrm{d}t} = J\boldsymbol{r}, \tag{25}$$

where $\vec{\rho}$ and $\boldsymbol{r}$ now stand for perturbation solutions, $\boldsymbol{G} = \nabla\vec{S}$ with respect to $\boldsymbol{r}$, $\boldsymbol{S}'$ is the Jacobian matrix of $\vec{S}$ with respect to $\vec{\rho}$, and J denotes the Jacobian matrix on the right-hand side of (23). For example, in 3D, we have the symmetric matrix

$$J = \begin{pmatrix} \zeta_{xx} & \zeta_{xy} & \zeta_{xz} \\ \zeta_{xy} & \zeta_{yy} & \zeta_{yz} \\ \zeta_{xz} & \zeta_{yz} & \zeta_{zz} \end{pmatrix}, \quad \zeta = \lambda_1\rho_1 + \lambda_2\rho_2 - \lambda_3\rho_3.$$

Because J is composed of bounded second derivatives, it makes sense to assume that $\tau||J|| \leqslant 1$ for step sizes τ which are realistic with respect to accuracy. Hence, we can say that the gradient equation is nonstiff and can be integrated explicitly. A practical reason to always choose for explicit integration of the semi-discrete gradient equation is the use of local piecewise interpolation. A consequence of local interpolation is that during integration we have to make updates when we pass a grid cell boundary. Updating renders no problem for an explicit method, but is not advocated within implicit integration using modified Newton iteration because the Jacobian matrix of the semi-discrete system is not continuous across grid cell boundaries.

In spite of the fact that $||J||$ is of moderate size, a standard explicit integrator may eventually become inefficient in a march to steady state during which we would like to steadily increase τ. This holds even stronger for the parabolic problem because the Laplacian gives rise to stiffness, something which manifests itself already in the transient phase. Hence, the parabolic problem cannot be efficiently integrated with a standard explicit method. In the current application, we may assume that both $||\boldsymbol{S}'||$ and $||\boldsymbol{G}||$ are of moderate size, similar as $||J||$.

Next, we will impose two further simplifying assumptions on (24) and (25). First, we assume that we may decouple the three parabolic equations. Specifically, the Jacobian matrix $\boldsymbol{S}'$ is supposed to be similar to a real-valued diagonal matrix with a real-valued, well-conditioned eigensystem. For stability investigations we then may replace (24) and (25) by

$$\frac{\partial \rho}{\partial t} = d\,\Delta\rho + G\cdot\boldsymbol{r} + S_\rho\rho, \tag{26}$$

$$\frac{\mathrm{d}\boldsymbol{r}}{\mathrm{d}t} = J\boldsymbol{r}, \tag{27}$$

where ρ is a scalar, S_ρ represents an eigenvalue of $\boldsymbol{S}'$ and G a transformed gradient vector, both real-valued and of moderate size. Second, we also assume that we may diagonalize J and replace (26) and (27) by the model system

$$\frac{\partial \rho}{\partial t} = d\,\Delta\rho + G\cdot\boldsymbol{s} + S_\rho\rho, \tag{28}$$

$$\frac{\mathrm{d}\boldsymbol{s}}{\mathrm{d}t} = D\boldsymbol{s}, \tag{29}$$

where D is the eigenvalue matrix of J and, using the same notation, G a new transformed gradient vector, still real-valued and of moderate size.

The same exercise can be carried out for the associated semi-discrete problems. Using the same notations G and S_ρ, the semi-discrete version of model (28)–(29) is written as

$$\frac{\mathrm{d}\rho_h}{\mathrm{d}t} = (d\,\Delta_h + S_\rho)\rho_h + G \cdot \boldsymbol{s}_h, \tag{30}$$

$$\frac{\mathrm{d}\boldsymbol{s}_h}{\mathrm{d}t} = D\boldsymbol{s}_h, \tag{31}$$

where the entries of D now represent derivatives of the interpolant P_{ρ_h}. Finally, we decompose ρ_h in Fourier modes,

$$\begin{pmatrix} \rho_h(\boldsymbol{x},t) \\ \boldsymbol{s}_h(t) \end{pmatrix} = \begin{pmatrix} c(t) \\ \boldsymbol{u}(t) \end{pmatrix} \cos(\omega \cdot \boldsymbol{x}),$$

so that we end up with the following model for linear time-stepping stability:

$$\frac{\mathrm{d}c}{\mathrm{d}t} = d_0 c + G \cdot \boldsymbol{u}, \tag{32}$$

$$\frac{\mathrm{d}\boldsymbol{u}}{\mathrm{d}t} = D\boldsymbol{u}, \tag{33}$$

where $d_0 = d\kappa + S_\rho$, κ being a real, negative eigenvalue of the discrete Laplacian Δ_h. Due to (16),

$$-\frac{64}{12}\frac{m}{h^2} \leqslant \kappa \leqslant 0. \tag{34}$$

In the remainder, we will denote the entries of D and G^{T} by d_k and g_k and hence use the notations $D = \mathrm{diag}(d_1, \ldots, d_m)$ and $G^{\mathrm{T}} = [g_1, \ldots, g_m]$.

In this model, $c \in \mathbb{R}$ represents a concentration and $\boldsymbol{u} \in \mathbb{R}^m$ a position. For the sake of the stability analysis, we assume that all eigenvalues d_k $(0 \leqslant k \leqslant m)$ are nonpositive. Of importance is that d_0 can take on very large negative values according to (34) (stiffness), while the gradient vector G and the diagonal matrix D are of moderate size. During transient phases stiffness thus only emerges from the 'parabolic' term $d_0 c$.

To a large extent the stability analysis of the model (32) and (33) is the same as for a single parabolic equation. However, as we will see in the next section, there is a difference due to the coupling with the gradient equation. Therefore, any method for mixed parabolic–gradient systems must pass the stability test for this simplified test model.

5.1. Power boundedness for Runge–Kutta methods

In what follows, we write the real-valued, linear model system (32)–(33) as

$$\frac{\mathrm{d}U}{\mathrm{d}t} = AU, \quad U = \begin{pmatrix} c \\ \boldsymbol{u} \end{pmatrix}, \quad A = \begin{pmatrix} d_0 & G^{\mathrm{T}} \\ \boldsymbol{0} & D \end{pmatrix}. \tag{35}$$

The Runge–Kutta–Chebyshev method discussed later on in this paper belongs to the class of explicit Runge–Kutta methods. Hence, when applied to (35), it yields a linear recurrence relation

$$U_{n+1} = R(\tau A)\, U_n, \quad n = 0, 1, \ldots, \quad R(\tau A) = \sum_{j=0}^{s} c_j (\tau A)^j, \tag{36}$$

where U_n is the approximation at time $t = t_n$, τ is the step size, and R is the stability polynomial, assuming s stages. We associate stability with the concept of power boundedness. For a given step size τ, the matrix $R(\tau A)$ is power bounded if there exists a constant C such that

$$||R(\tau A)^n|| \leqslant C \quad \text{for all } n \geqslant 1. \tag{37}$$

Hence, C should exist independent of n and for practice C should of course be of moderate size. Trivially, power boundedness implies $||U_n|| \leqslant C||U_0||$ uniformly in n for the value of τ under consideration (stability).

We will derive a general expression for $R(\tau A)$, where $R(z)$ can be any polynomial or rational function or the exponential function. Consequently, the derived expression is also valid for stability functions generated by implicit Runge–Kutta or linearly implicit Runge–Kutta–Rosenbrock methods, as well as for the exact solution operator $\exp(\tau A)$. First, let d_0 be distinct from all entries d_k of the diagonal matrix D and compute the eigenvector–eigenvalue decomposition $A = X \Lambda X^{-1}$,

$$\Lambda = \begin{pmatrix} d_0 & \mathbf{0}^{\mathrm{T}} \\ \mathbf{0} & D \end{pmatrix}, \quad X = \begin{pmatrix} 1 & G^{\mathrm{T}}(D - d_0 I)^{-1} \\ \mathbf{0} & I \end{pmatrix}, \tag{38}$$

$$X^{-1} = \begin{pmatrix} 1 & -G^{\mathrm{T}}(D - d_0 I)^{-1} \\ \mathbf{0} & I \end{pmatrix}.$$

Elaborating $R(\tau A) = X\, R(\tau \Lambda) X^{-1}$ gives

$$R(\tau A) = \begin{pmatrix} R(\tau d_0) & V^{\mathrm{T}} \\ \mathbf{0} & R(\tau D) \end{pmatrix}, \quad V^{\mathrm{T}} = [v_1, \ldots, v_m], \tag{39}$$

where

$$v_k = \tau g_k (\tau d_k - \tau d_0)^{-1} (R(\tau d_k) - R(\tau d_0)). \tag{40}$$

With the mean value theorem we can write v_k also as $v_k = \tau g_k R'(\tau \tilde{d}_k)$, where $d_0 \leqslant \tilde{d}_k \leqslant d_k$. Next, suppose that d_0 equals one or more of the entries d_k of D. The above derivation then still can be used when accompanied with a standard limit argument. Specifically, if $d_0 = d_k$, then

$$v_k = \tau g_k R'(\tau d_k). \tag{41}$$

The powers of $R(\tau A)$ read

$$R(\tau A)^n = \begin{pmatrix} R(\tau d_0)^n & W^{\mathrm{T}} \\ \mathbf{0} & R(\tau D)^n \end{pmatrix}, \quad W^{\mathrm{T}} = [w_1, \ldots, w_m], \tag{42}$$

where

$$w_k = v_k \sum_{i=0}^{n-1} R(\tau d_k)^i R(\tau d_0)^{n-i-1}. \tag{43}$$

Inserting expressions (40) and (41) yields

$$w_k = \begin{cases} \tau g_k (\tau d_k - \tau d_0)^{-1} (R^n(\tau d_k) - R^n(\tau d_0)) & \text{if } d_0 \neq d_k, \\ n\tau g_k R'(\tau d_k) R^{n-1}(\tau d_k) & \text{if } d_0 = d_k, \end{cases} \tag{44}$$

or

$$w_k = \begin{cases} n\tau g_k R'(\tau \tilde{d}_k) R^{n-1}(\tau \tilde{d}_k), d_0 \leqslant \tilde{d}_k \leqslant d_k & \text{if } d_0 \neq d_k, \\ n\tau g_k R'(\tau d_k) R^{n-1}(\tau d_k) & \text{if } d_0 = d_k. \end{cases} \tag{45}$$

These inequalities are valid for $R(\tau A) = e^{\tau A}$ and for $R(\tau A)$ generated by stability functions $R(z)$. Due to consistency, $R(z) = e^z + O(z^2)$ for $z \to 0$. Hence, for $z = \tau d_k$ $(0 \leqslant k \leqslant m)$ close to zero, $R(n\tau A)$ will be close to $e^{n\tau A}$ in the sense that the bound C introduced in definition (37) will be close to 1. For values not close to zero the situation is different because stability functions decay much slower than the exponential, or do not decay at all. However, for power boundedness decay is not necessary. With a minor exception it is sufficient (see Theorem 1) that all values τd_k $(0 \leqslant k \leqslant m)$ belong to the real stability interval $[-\beta, 0]$, $\beta = \max(z_\beta : |R(z)| \leqslant 1, -z_\beta \leqslant z \leqslant 0)$, which is the common (scalar) stability requirement.

Remark. Here we see the difference of the stability analysis for parabolic equations with and without coupling to a gradient equation. This is exemplified by formula (45) where we observe potential linear growth with n for a fixed step size τ. Hence, the coupling term $G \cdot \mathbf{u}$ in (32) is relevant in the stability analysis. The linear growth must be counterbalanced by $R^{n-1}(\tau d_k)$ which suggests to choose time integration methods providing some damping. The Runge–Kutta–Chebyshev method can be applied with damping and will be discussed in Section 6.

Lemma 1. *Suppose $R(z)$ is damped for $\tau d_0 \leqslant z \leqslant \tau d_k$, i.e., $|R(z)| \leqslant \eta < 1$. Then, for all $n \geqslant 1$,*

$$|w_k| \leqslant \left| \frac{\tau g_k R'(\tau \tilde{d}_k)}{e\eta \ln \eta} \right|, \quad d_0 \leqslant \tilde{d}_k \leqslant d_k. \tag{46}$$

Proof. Imposing $|R(z)| \leqslant \eta$ in (45) yields $|w_k| \leqslant n\tau\eta^{n-1} |g_k R'(\tau \tilde{d}_k)|$, where $d_0 \leqslant \tilde{d}_k \leqslant d_k$. The positive function $f(x) = x\eta^{x-1}$, $x \geqslant 1$, vanishes for $x \to \infty$ and has a maximum at $x = -1/\ln \eta$. This maximum is given by $-1/(e\eta \ln \eta)$. □

Theorem 1. *The amplification matrix $R(\tau A)$ is power bounded if all values τd_k $(0 \leqslant k \leqslant m)$ belong to the real stability interval $[-\beta, 0]$ and none of the pairs $\tau d_0, \tau d_k$ $(1 \leqslant k \leqslant m)$ coalesce at the boundary.*

Proof. Because $|R(\tau d_k)| \leqslant 1$ $(0 \leqslant k \leqslant m)$, we have power boundedness if the entries w_k are bounded uniformly in n. First suppose $d_0 \neq d_k$. Boundedness of w_k then follows immediately from (44). Second, suppose $d_0 = d_k$. By assumption, $z = \tau d_0$ then lies in the interior of the stability interval. Now two situations can occur, either $|R(z)| \leqslant \eta < 1$ or $|R(z)| = 1$. If $|R(z)| \leqslant \eta < 1$, Lemma 1 applies so that w_k is bounded. If $|R(z)| = 1$, then $R'(z) = 0$ because z belongs to the interior of the stability interval and $|R(z)| = 1$ is an extremum. In this situation $w_k = 0$. □

Remark. Suppose that $\tau > 0$ and that $d_0 = d_k = 0$. Then $\tau d_0, \tau d_k$ coalesce at the boundary point $z = 0$. Because $R(0) = R'(0) = 1$, we then get $w_k = n\tau g_k$ (cf. (45)) which increases without bound with n. However, also the exact solution increases linearly with time and hence the case $d_0 = d_k = 0$ is of no interest and should be excluded in a stability analysis. Next suppose that $\tau d_0, \tau d_k$ coalesce at the other boundary point $z = -\beta$ and that β is finite. By definition, then $|R(-\beta)| = 1$ so that in this case $|w_k| = n\tau |g_k R'(-\beta)|$ which is also unbounded. Hence, in this special case uniform boundedness of $R(\tau A)$ does not exist. Theorem 1 therefore excludes it. Would β be infinite and $|R(-\beta)| = 1$, the eigenvalues are allowed to coalesce because at infinity R' vanishes.

6. The Runge–Kutta–Chebyshev method

We proceed with the explicit Runge–Kutta–Chebyshev method. This method is intended for solving systems of ordinary differential equations

$$\frac{\mathrm{d}U}{\mathrm{d}t} = F(U), \quad t > 0, \quad U(0) = U_0, \tag{47}$$

which possess a 'close-to-normal' Jacobian matrix $F'(U)$ with eigenvalues located in a long, narrow band along the negative axis in the complex plane. In the present application it is the Laplace operator that counts. Since the Laplacian gives rise to a real, negative spectrum, RKC is a suitable candidate. Another reason for choosing RKC is that we wish to integrate the nonstiff gradient equation by means of an explicit method. In this section, we will discuss the integration formula, its stability properties, and we will discuss two numerical tests.

6.1. The integration formula

RKC is based on the s-stage formula

$$\begin{aligned}
&Y_0 = U_n,\\
&Y_1 = Y_0 + \tilde{\mu}_1 \tau F_0,\\
&Y_j = (1 - \mu_j - \nu_j) Y_0 + \mu_j Y_{j-1} + \nu_j Y_{j-2} + \tilde{\mu}_j \tau F_{j-1} + \tilde{\gamma}_j \tau F_0, \quad j = 2, \ldots, s,\\
&U_{n+1} = Y_s,
\end{aligned} \tag{48}$$

where $F_j = F(Y_j)$. All the coefficients are available in analytical form for arbitrary $s \geqslant 2$. They are defined as follows. Let T_j be the Chebyshev polynomial of the first kind of degree j satisfying the three-term recursion $T_0(x) = 1, T_1(x) = x, T_k(x) = 2xT_{k-1}(x) - T_{k-2}(x)$, $2 \leqslant k \leqslant j$. Defining

$$\varepsilon = \frac{2}{13}, \quad w_0 = 1 + \varepsilon/s^2, \quad w_1 = \frac{T_s'(w_0)}{T_s''(w_0)}, \quad b_j = \frac{T_j''(w_0)}{(T_j'(w_0))^2} \quad (2 \leqslant j \leqslant s),$$

and $b_0 = b_2$, $b_1 = b_2$, the coefficients are given by

$$\tilde{\mu}_1 = b_1 w_1, \quad \mu_j = \frac{2b_j w_0}{b_{j-1}}, \quad \nu_j = \frac{-b_j}{b_{j-2}}, \quad \tilde{\mu}_j = \frac{2b_j w_1}{b_{j-1}},$$

$$\tilde{\gamma}_j = -(1 - b_{j-1} T_{j-1}(w_0)) \tilde{\mu}_j \quad (2 \leqslant j \leqslant s).$$

The stage formula computing Y_j is reminiscent of the three-term Chebyshev recursion [8]. All approximations $Y_j\,(2 \leqslant j \leqslant s)$ are second-order consistent [14] and the real stability boundary β is very close to $0.65s^2$. Hence, β is quadratic in s. Noteworthy is that s can vary and that s can be made arbitrarily large so as to fulfil the linear stability requirement for a chosen step size τ. This makes it possible for RKC to select at each step the most efficient step size (maximal τ) defined by local error control [11], as well as the most efficient stable formula (minimal s). This also makes it attractive to use RKC for a march to steady state, provided s can be kept within reasonable bounds for efficiency. Moreover, RKC evaluates the explicit formulas in just a few vectors of storage, which can be of interest for parabolic problems in several spatial variables. For more details we refer to the original paper [8], the survey paper [14], and the software paper [11] where a FORTRAN code is discussed. We will illustrate this code in Section 6.4.2.

6.2. The stability polynomial

The stability polynomial of the s-stage RKC method is the Bakker–Chebyshev polynomial $R(z) = 1 - b_s T_s(w_0) + b_s T_s(w_0 + w_1 z)$ [14] for which

$$\beta = \frac{(w_0 + 1)T_s''(w_0)}{T_s'(w_0)} \approx \frac{2}{3}(s^2 - 1)\left(1 - \frac{2}{15}\varepsilon\right). \tag{49}$$

The parameter ε has been introduced to obtain damping. Would we choose $\varepsilon = 0$, then $R(z)$ alternates between $\approx \frac{1}{3}$ and 1 as long as z lies in the stability interval $[-\beta, 0]$. That means that at isolated points z we have $R(z) = 1$. For $0 < \varepsilon \ll 1$, the RKC polynomial is damped, i.e., $|R(z)| \leqslant \eta < 1$ on a subinterval $[-\beta_l, -\beta_r] \subset [-\beta, 0]$ such that $\beta_l \approx \beta$ and $\beta_r \approx 0$. The value $\varepsilon = \frac{2}{13}$ gives approximately 5% damping (see Section 6.3), letting $R(z)$ alternate between $\approx \frac{1}{3}$ and $\eta = 0.95$ for $z \in [-\beta_l, -\beta_r]$. For this value of ε, the boundary $\beta \approx 0.65s^2$. Fig. 2 illustrates this damped case for $s = 10$. Note that β_l and β_r are the values of z where $R(z)$ intersects the upper dashed line.

6.3. Power boundedness

According to Theorem 1, RKC will be power bounded as long as $z = \tau d_k$ $(0 \leqslant k \leqslant m)$ belongs to the stability interval $[-\beta_l, 0]$, which is only slightly smaller than $[-\beta, 0]$ (see, e.g., Fig. 2). To be more specific about RKC, we now wish to apply Lemma 1 and are therefore going to specify the exact amount of damping over $[-\beta_l, 0] = [-\beta_l, -\beta_r] \cup [-\beta_r, 0]$.

By construction, the point β_r is determined by the condition $R(-\beta_r) = \eta$ at the right end point of the Chebyshev interval $[-1, 1]$. Hence,

$$\beta_r = \frac{w_0 - 1}{w_1} = \frac{\varepsilon T_s''(w_0)}{s^2 T_s'(w_0)}.$$

Inserting $T_s'(1) = s^2$, $T_s''(1) = \frac{1}{3}s^2(s^2 - 1)$, $T_s'''(1) = \frac{1}{15}s^2(s^2 - 1)(s^2 - 4)$ and expanding in ε yields

$$\beta_r = \frac{1}{3}\frac{s^2 - 1}{s^2}\varepsilon\left[1 - \varepsilon\frac{2s^2 + 7}{15s^2} + O(\varepsilon^2)\right] \approx \tfrac{1}{3}\varepsilon.$$

Let $\eta = 1 - \mu$. By construction, $a_s + b_s = 1 - \mu$. Hence,

$$\mu = \frac{T_s''(w_0)}{(T_s'(w_0))^2}(T_s(w_0) - 1).$$

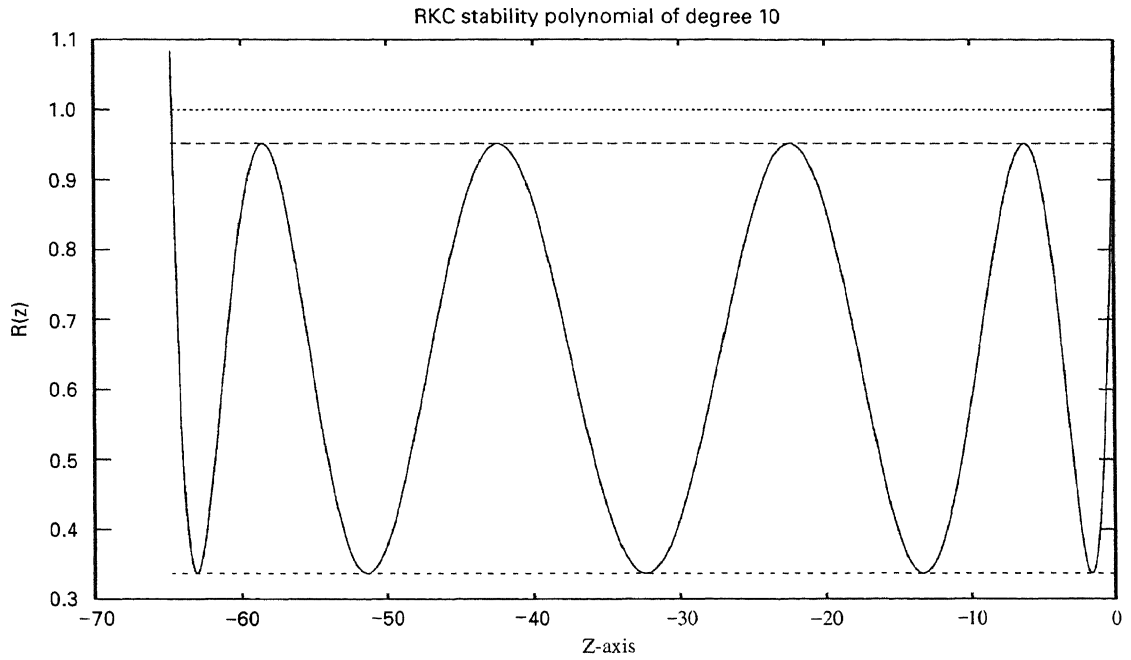

Fig. 2. The stability polynomial $R(z)$ of degree 10 along the stability interval $-65 \leqslant z \leqslant 0$.

Expanding in ε, similar as for β_r, yields

$$\mu = \tfrac{1}{3}\frac{s^2-1}{s^2}\varepsilon\left[1 - \varepsilon\frac{3s^2+3}{10s^2} + O(\varepsilon^2)\right] \approx \tfrac{1}{3}\varepsilon.$$

We see that for $s \geqslant 2$ and ε sufficiently small, $\mu/\beta_r < 1$ (this holds for $\varepsilon = \frac{2}{13}$). Specifically,

$$\frac{\mu}{\beta_r} = 1 - \tfrac{1}{6}\varepsilon\frac{s^2-1}{s^2} + O(\varepsilon^2).$$

Because $R'(0) = 1$ and $R(z)$ is convex for $z \in [-\beta_r, 0]$, on this interval we can bound $R(z)$ by the straight line $1 + (\mu/\beta_r)z$. On the whole of the stability interval $[-\beta_l, 0]$ this results in

$$|R(z)| \leqslant \eta = \begin{cases} \approx 1 - \varepsilon/3 \approx 0.95 & \text{for } -\beta_l \leqslant z \leqslant -\beta_r, \\ 1 + (\mu/\beta_r)z \approx 1 + z & \text{for } -\beta_r \leqslant z \leqslant 0. \end{cases} \tag{50}$$

This result enables us to specify bounds for the entries w_k occurring in $R(\tau A)^n$. First, suppose τd_0 and τd_k both belong to the interval $[-\beta_l, -\beta_r]$. We then can apply Lemma 1 with $\eta \approx 1-\varepsilon/3 \approx 0.95$. By also taking into account $|R'(z)| \leqslant 1$ for z in the stability interval, we obtain

$$|w_k| \leqslant \left|\frac{\tau g_k R'(\tau\tilde{d}_k)}{e\eta \ln \eta}\right| \leqslant \left|\frac{\tau g_k}{e\eta \ln \eta}\right| \approx 7.6\tau|g_k|. \tag{51}$$

Of interest is that this bound applies for the greater part of the stability interval, since $\beta_r \approx \varepsilon/3 \approx 0.05$ is very close to the origin.

Obviously, on the remaining small interval $[-\beta_r, 0]$, all consistent Runge–Kutta methods have a bound for $R(\tau A)^n$ very close to that of the true solution operator $e^{\eta\tau A}$. Suppose $z = \tau d_0$ or $z = \tau d_k$ belongs to this small interval and that they do not coalesce at $z = 0$. Let $z = \tau d_k$ be the value closest to the origin. We then can apply Lemma 1 with $\eta = 1 + (\mu/\beta_r)z$. This yields

$$|w_k| \leqslant \left| \frac{\tau g_k R'(\tau d_k)}{e\eta \ln \eta} \right| \leqslant \left| \frac{\tau g_k}{e\eta \ln \eta} \right| \approx \left| \frac{g_k}{e d_k} \right|. \tag{52}$$

This bound gets larger as d_k is closer to the origin. The bound is strict if $d_0 = d_k$, reflecting the lack of boundedness if the eigenvalues coalesce at the origin.

6.3.1. Example

On fine space grids the largest eigenvalue is d_0. According to (34), $d_0 \approx -\frac{64}{12}\frac{dm}{h^2}$, so that for (32)–(33) we have power boundedness if

$$\tau \leqslant \frac{0.65 s^2}{|d_0|} \approx \frac{7.8 h^2 s^2}{64 dm}. \tag{53}$$

The test problem from Section 4.1 has $d = 2.0 \cdot 10^{-4}$ and $m = 2$. Hence, when using the 80×80 space grid, we have to satisfy the inequality $\tau \leqslant s^2/21.005$. The 320×320 grid yields the inequality $\tau \leqslant s^2/336.08$. A very valuable property of RKC is that it can be applied with any value of s. For actual computation we may therefore suppose that τ is determined by accuracy considerations based on local error control [11] and that s is adjusted for stability. For the two mentioned grids this means $s \approx \sqrt{21.005\tau}$ and $s \approx \sqrt{336.08\tau}$. These numbers of derivative evaluations give an indication for the amount of work that RKC will need per time step in axonal growth calculations.

6.4. Numerical illustrations

6.4.1. Convergence for the gradient equations

The ODE system $\dot{U} = F(U)$ to which RKC is applied contains all semi-discrete parabolic and gradient equations present in the model. The gradient equation components of $F(U)$ are defined by the piecewise Hermite interpolation procedure discussed in Sections 3 and 4. Let Eq. (19) be such a component. By construction, its solution $\boldsymbol{r}_h$ and the first derivative $\dot{\boldsymbol{r}}_h$ exist and are continuous in t. Also the second derivative $\ddot{\boldsymbol{r}}_h$ exists, but this second derivative is discontinuous at the crossing of a grid cell. When this happens, the second-order consistency of RKC reduces to one, causing some loss of accuracy. Because on a given grid the number of grid cell crossings is finite, the effect of the order reduction will diminish when the number of time steps increases. Specifically, for $\tau \to 0$ the method is still second-order convergent, because only a finite number of local errors of $O(\tau^2)$ exist. When the spatial grid size is reduced, the number of grid cell crossings will increase, resulting in a larger-order reduction.

We illustrate the temporal convergence behaviour of RKC for the test problem of Section 4.1. To emphasize the (minor) order reduction phenomenon, the very fine 320×320 grid has been used. Table 2 shows temporal errors for a number of fixed step sizes and associated convergence orders. We have also listed s, the number of stages, which can be computed from (53). It can be concluded that RKC converges as expected. Because the source term of the parabolic equation does not depend on the gradient equation solutions, the convergence behaviour for ρ_h is standard. For the gradient

Table 2
Maximum norm errors for RKC for the problem of Section 4.1, $t = 45$, $h = \frac{1}{320}$

No. of steps	s	$\|\|(\rho - \rho_h)(45)\|\|$	Order	$\|\|(r_n - r_{n,h})(45)\|\|$	Order
50	18	$0.463 \cdot 10^{-4}$		$0.622 \cdot 10^{-2}$	
100	13	$0.116 \cdot 10^{-4}$	1.99	$0.197 \cdot 10^{-2}$	1.66
200	9	$0.295 \cdot 10^{-5}$	1.98	$0.567 \cdot 10^{-3}$	1.80
400	7	$0.762 \cdot 10^{-6}$	1.95	$0.155 \cdot 10^{-3}$	1.87

equations the order is only slightly smaller than two and the minor reduction diminishes when the number of time steps increases.

6.4.2. *The FORTRAN code RKC illustrated*

RKC has been coded in a FORTRAN program, also named RKC [11]. This code works as a variable step size ODE solver using local error control. In addition, to minimize work, at each step it selects the minimal number of stages s for stability. In the actual application s may increase to very large values. Algorithmically, s is only constrained by internal growth of round-off proportional to s^2. For a very large number of stages, RKC can of course no longer be considered efficient. A great advantage is that it is explicit. Hence, programming is easy and adding or deleting equations in a model is straighforward for implementations.

Focusing again on target attraction, we have applied the code to the test problem of Section 4.1, except that now the source is switched off when the target has nearly been reached. Our purpose is to illustrate the code's ability to approach a complete steady state with larger and larger step sizes. For switching off the source, we have used the condition

$$\sum_{n=1}^{10} \text{dist}\,(r_{n,h}(t) - (\tfrac{1}{2}, \tfrac{1}{2})) < 0.1,$$

which is satisfied at $t \approx 46$. The integration is continued up to $t = 200$ which is sufficiently far. The effect of switching off the source is that the bell-shaped solution for ρ slowly smooths out.

To illustrate the reliability of RKCs variable (τ, s)-strategy, we have used two space grids, 80×80 and 320×320. Fig. 3 shows for both grids the step size history for a tolerance value $\text{TOL} = 10^{-4}$. Hardly any difference exists, indicating that the (τ, s)-strategy works fine. This is further exemplified by Table 3 which contains maximum norm temporal errors[1] at $t = 45$ for different values of TOL. The table also contains standard integration statistics. One can see that there is hardly any difference in temporal accuracy and number of time steps for the coarse and the fine grid. On the fine grid, the number of function evaluations is about four times larger, completely in accordance with (53). On the fine grid, the average number of (explicit derivative) evaluations per time step is, for example, equal to 14 for $\text{TOL} = 10^{-5}$. In view of the fact that we are solving a parabolic equation and gradient equations, this work load is still moderate. Of further interest is that the step size and local error

[1] The code described in [11] uses the weighted Euclidean norm for the local error estimation. For the current test, we have adapted the code to use the maximum norm to impose a more stringent test for the gradient equations. Observe that the factor of $\frac{1}{15}$ in the formula for Est_{n+1} in [11] must be replaced by $\frac{1}{27}$ to have $Est_{n+1} = Le(t_{n+1}) + O(\tau^4)$. This correction is not essential for the application of the code. Our tests have been carried out with the factor $\frac{1}{15}$.

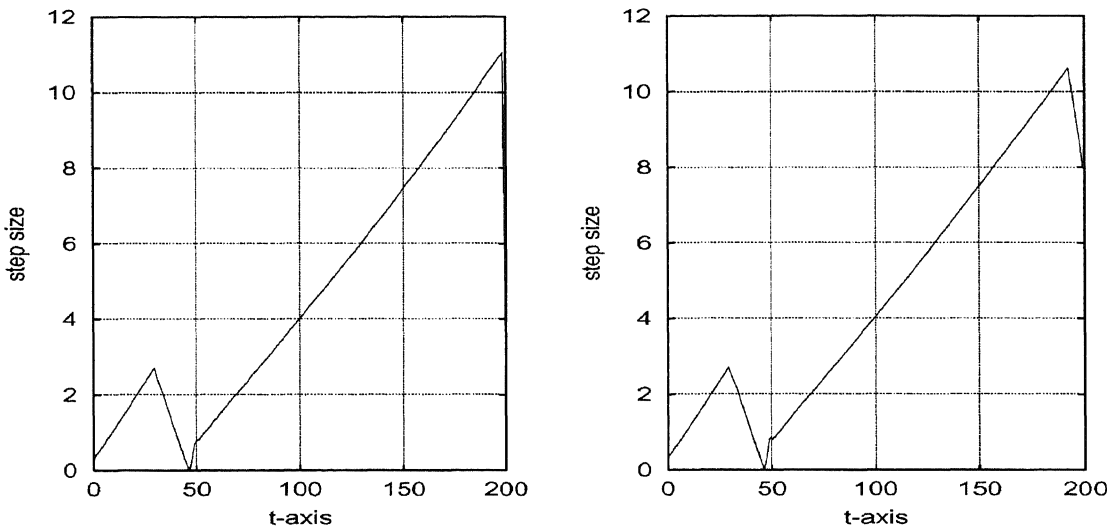

Fig. 3. Step size plots for the experiment of Section 6.4.2; at the left for the 80 × 80 grid, at the right for the 320 × 320 grid. Close to $t = 200$ the step size τ has been automatically reduced to hit this end point exactly.

Table 3
Integration results for the experiment of Section 6.4.2. At time $t = 200$ the solution is very close to steady state so that the temporal errors are extremely small at this point of time. Therefore, we only give the temporal errors for $t = 45$

t_{end}	TOL	$\|\|\rho - \rho_h\|\|$	$\|\|r_n - r_{n,h}\|\|$	Steps	Acc.	Rej.	F-evals	s_{max}
Maximum norm errors and integration statistics on 80 × 80 *grid*								
45	10^{-2}	$0.386 \cdot 10^{-2}$	$0.482 \cdot 10^{-1}$	13	11	2	128	16
	10^{-3}	$0.835 \cdot 10^{-3}$	$0.204 \cdot 10^{-1}$	23	22	1	159	12
	10^{-4}	$0.172 \cdot 10^{-3}$	$0.550 \cdot 10^{-2}$	48	47	1	237	8
	10^{-5}	$0.385 \cdot 10^{-4}$	$0.138 \cdot 10^{-2}$	103	103	0	365	6
200	10^{-2}	—	—	34	31	3	354	29
	10^{-3}	—	—	64	58	6	468	21
	10^{-4}	—	—	126	118	8	684	16
	10^{-5}	—	—	261	250	11	1052	11
Maximum norm errors and integration statistics on 320 × 320 *grid*								
45	10^{-2}	$0.376 \cdot 10^{-2}$	$0.473 \cdot 10^{-1}$	13	11	2	490	65
	10^{-3}	$0.800 \cdot 10^{-3}$	$0.188 \cdot 10^{-1}$	23	22	1	591	49
	10^{-4}	$0.161 \cdot 10^{-3}$	$0.499 \cdot 10^{-2}$	47	46	1	833	32
	10^{-5}	$0.341 \cdot 10^{-4}$	$0.118 \cdot 10^{-2}$	97	97	0	1187	21
200	10^{-2}			34	30	4	1373	106
	10^{-3}			64	56	8	1746	86
	10^{-4}			115	111	4	2388	60
	10^{-5}			251	238	13	3496	43

control can be seen to obey the theory given in Shampine [10, p. 339]. This theory says that upon reducing TOL by 10, the global error will asymptotically decrease by $10^{p/(p+1)}$. For $p=2$, the order of consistency of RKC, this gives a factor of about 5, which we can trace in Table 3.

7. Possible future research

This paper deals with migration in gradient fields described by a model from neuroscience. In this model, the gradient fields are solutions of parabolic equations with source terms representing concentrations of biochemicals. Similar migration problems occur in other biological applications (see, e.g., [5]). The numerical solution we have discussed rests on a combination of efficient existing techniques, piecewise cubic Hermite interpolation, the fourth-order finite differencing, and the second-order time integration by an explicit RKC method especially designed for parabolic problems. We have shown that this combination works well and that it can be used for solving a wide range of mixed parabolic–gradient systems.

This paper is the first in a co-operation with the Netherlands Institute for Brain Research in the field of computational neuroscience. The long-term goal is further model and algorithm development focusing on axonal growth. What comes to mind for further numerical research includes (1) treatment of highly localized source terms on grids, (2) biquadratic or even quintic piecewise Hermite interpolation or global spectral or spline collocation methods [3,6] for obtaining smoother gradient equation solutions, (3) higher-order time stepping methods to exploit this, e.g., special purpose implicit–explicit methods [1,2] or Rosenbrock methods using approximate or factorized Jacobian matrices [15], (4) adaptivity and local refinement in the vicinity of steep gradients and near the trajectories, and (5) the efficient treatment of systems assuming a quasi-steady state for the parabolic equations.

Acknowledgements

We thank Arjen van Ooyen and Jaap van Pelt from the Netherlands Institute for Brain Research for helpful discussions on the kind of models used in studying axonal growth.

References

[1] U.M. Ascher, S.J. Ruuth, B. Wetton, Implicit–explicit methods for time-dependent PDEs, SIAM J. Numer. Anal. 32 (1995) 797–823.
[2] U.M. Ascher, S.J. Ruuth, R.J. Spiteri, Implicit–explicit Runge–Kutta methods for time-dependent partial differential equations, Appl. Numer. Math. 25 (1997) 151–167.
[3] B. Bialecki, R.I. Fernandes, An orthogonal spline collocation alternating direction implicit Crank–Nicolson method for linear parabolic problems on rectangles, SIAM J. Numer. Anal. 36 (1999) 1414–1434.
[4] C. de Boor, A Practical Guide to Splines, Applied Mathematical Sciences, Vol. 27, Springer, Berlin, 1978.
[5] J.C. Dallon, Numerical aspects of discrete and continuum hybrid models in cell biology, Appl. Numer. Math. 32 (2000) 137–159.
[6] G. Fairweather, D. Meade, Spline collocation method for the numerical solution of differential equations, in: I.C. Diaz (Ed.), Math. for Large Scale Computing, Lect. Notes in Pure and Applied Math., Vol. 120, Dekker, New York, 1989, pp. 297–341.

[7] H.G.E. Hentschel, A. van Ooyen, Models of axon guidance and bundling during development, Proc. R. Soc. Lond. B. 266 (1999) 2231–2238.
[8] P.J. van der Houwen, B.P. Sommeijer, On the internal stability of explicit m-stage Runge–Kutta methods for large values of m, ZAMM 60 (1980) 479–485.
[9] A. van Ooyen, Personal communication, Netherlands Institute for Brain Research, Amsterdam, 1999.
[10] L.F. Shampine, Numerical Solution of Ordinary Differential Equations, Chapman & Hall, New York, 1994.
[11] B.P. Sommeijer, L.F. Shampine, J.G. Verwer, RKC: An explicit solver for parabolic PDEs, J. Comput. Appl. Math. 88 (1997) 315–326.
[12] M.H. Schultz, Spline Analysis, Prentice-Hall, Englewood Cliffs, NJ, 1973.
[13] A.M. Stuart, A.R. Humphries, Dynamical Systems and Numerical Analysis, Cambridge University Press, Cambridge, 1996.
[14] J.G. Verwer, Explicit Runge–Kutta methods for parabolic partial differential equations, Appl. Numer. Math. 22 (1996) 359–379.
[15] J.G. Verwer, E.J. Spee, J.G. Blom, W. Hundsdorfer, A second order Rosenbrock method applied to photochemical dispersion problems, SIAM J. Sci. Comput. 20 (1999) 1456–1480.